Case Studies in Construction Materials 23 (2025) e05149

Contents lists available at ScienceDirect

Case Studies in Construction Materials

journal homepage: www.elsevier.com/locate/cscm

Tuning interfacial properties of C-A-S-H gels through Al/Si ratio control: Multiscale simulation insights

Wenhao Xia [a], Yihan Wang [a], Pan Wang [a], Yue Zhang [a], Dongshuai Hou [a], Muhan Wang [a,b,*], Xiangming Zhou [b,**]

[a] Department of Civil Engineering, Qingdao University of Technology, Qingdao 266033, China
[b] Department of Civil & Environmental Engineering, Brunel University London, Uxbridge, Middlesex UB8 3PH, UK

ARTICLE INFO

Keywords:
Interfacial tension
CASH gel
Al/Si Ratio
Molecular dynamics simulation
Quantum chemical calculation
Concrete durability

ABSTRACT

Understanding the role of aluminum incorporation in calcium-aluminosilicate-hydrate (CASH) gels is crucial for enhancing cement-based materials' durability. The presented research employs molecular dynamics simulations and quantum chemical calculations to examine how changing the Al/Si ratio affects the interfacial tension of CASH gels with water. The results reveal that initial aluminum addition increases interfacial tension, while further increases in the Al/Si ratio lead to a gradual reduction, indicating an optimal aluminum content for minimizing solution transport. Analysis of the interface microstructure and lamellar interfacial tension suggests that increased Al/Si ratios contribute to a more homogeneous interface. Molecular interaction analysis shows that calcium is a key factor in interfacial bonding, with aluminum enhancing calcium adsorption and inhibiting its detachment. Quantum chemical analysis confirms that calcium adsorption occurs via electrostatic interactions, with weaker electron localization in aluminum-containing structures. These findings shed light on the mechanism by which aluminum in CASH gels inhibits transportation at the molecular level, offering valuable guidance for designing durable concrete materials.

1. Introduction

Durability is a crucial performance characteristic for concrete structures, which significantly affects the long service-life design of infrastructure, such as bridges, offshore platforms, tunnels, et al. [1,2]. Concrete structures are inevitably exposed to corrosive mediums in natural environments such as the atmosphere, rain, and, most importantly, seawater [3,4]. Harmful substances will transport the pores of concrete along with the seawater medium and cause corrosion or deterioration, thus threatening durability. These pores originate from the development of cement hydration product that is mainly consisted by Calcium-Silicate-Hydrate (CSH) and also decide the transportation process [5,6]. The corrosion or deterioration of reinforcement concrete will unavoidably occur once the transportation has occurred [7]. Therefore, controlling solution transport within the nanopores is an essential strategy for enhancing concrete durability.

To date, numerous methods have been proposed to regulate solution transport on concrete surfaces, which are generally divided into two primary groups: external surface modifications and internal microscopic treatments. Regarding the external surface, applying

* Corresponding author at: Department of Civil Engineering, Qingdao University of Technology, Qingdao 266033, China.
** Corresponding author.
E-mail addresses: wangmuhan@qut.edu.cn (M. Wang), xiangming.zhou@brunel.ac.uk (X. Zhou).

https://doi.org/10.1016/j.cscm.2025.e05149
Received 20 June 2025; Received in revised form 28 July 2025; Accepted 4 August 2025
Available online 6 August 2025

a hydrophobic treatment to reduce surface energy has proven to be an effective method for enhancing concrete durability by preventing solution transportation [8-10]. For instance, a continuous film of varying thickness, commonly referred to as a coating, can be applied to the concrete surface to restore its hydrophobic properties [11,12]. While this method performed well initially, the coating's degradation weakens the bond with the concrete, ultimately shortening the concrete's lifespan [13]. Moreover, on a microscopic scale, optimizing the nanoporous framework within cementitious materials enhances the concrete's internal density, thereby increasing its durability throughout its service life [14]. Compared with surface treatments, optimizing the internal microstructure offers a more effective solution for controlling solution transportation. Interestingly, research has shown that concrete's transportation properties can also be improved without substantial changes to its internal porosity [15–17]. Qomi et al. built a CASH model utilizing nuclear magnetic resonance (NMR) test results and confirmed that aluminum addition enhances the long-term stability of hydrated products [18]. Hou and Li investigated the transportation of NaCl solution in CASH gel's nanopores and found that, relative to movement through CSH pores, the migration rate of both water and ions is more slowly in CASH gel [19]. Hou et al. further examined how aluminate affects the transportation of water and ions within the nanoporous structure of CSH gel. They found that CASH gel is more effective at retaining sodium and chloride ions on its surface compared to CSH gel, leading to a 50 % reduction in the mobility of sodium ions confined within the nanopores [20]. It should be noteworthy that many commonly used supplementary cementitious materials (SCMs), including materials like coal combustion residues and slag from ironmaking processes, are rich in aluminum [21, 22]. Replacing part of the cement with SCMs during concrete production not only reduces CO_2 emissions but also enhances the concrete's durability [23–25]. However, the challenge is how the addition of the aluminum phase changes the transportation properties of concrete. Solving this issue will help the promotion of anti-transportation capabilities.

Solution transport in micro-/nano-pores primarily depends on permeation, which is influenced by the interfacial tension [26]. On the scale of molecules, interfacial tension is a result of energy difference between the substrate materials and the solution phase [27]. It is also accurately defined as the energy required to form an interface per unit area [27]. The presence of interfacial tension between the solution and the CSH gel leads to the development of negative capillary pressure inside the gel. This negative capillary pressure drives external solution into the gel's nanopores via the capillary permeation effect [28]. The resulting pressure gradient drives the migration of water and ions from the external environment into CSH gel, explaining the mechanism behind the permeation process. Therefore, the key to controlling solution transportation lies in investigating the influence of interfacial tension at the nanoscale.

Analyzing nanoscale interfacial tension can be effectively achieved through molecular dynamics (MD) simulations. MD simulations can not only illustrate the microscopic changes observed in macroscopic experiments, but also reveal the underlying mechanisms at the nanometer scale. Hou et al. modelled the wettability changes induced by the concentration of NaCl droplets on the CSH surface using the MD method, predicting the contact angle by calculating the interfacial tension between each droplet and the CSH gel [29]. Yang simulated the interfacial tension between CSH and three other materials, and assessed the bonding performance at the interface using stress–strain analysis [30]. Additionally, several studies have focused on using MD simulations to calculate interfacial tension in order to explore the strength of interfacial bonding between different materials [31–33]. However, it should be noted that these studies have primarily explored specific values of interfacial tension through MD simulations, with few investigating the hierarchical variations of interfacial tension. Furthermore, variations in interfacial tension strength between water and CASH gel remain unexplored in existing research. Therefore, this study investigates the interfacial tension between CASH gel and water at various aluminum to silicon ratios using MD simulation method. The findings demonstrate that the aluminum phase will increase the interfacial tension in the pores and thus prevent the transportation process of solution. The introduction of aluminum results in an increase in the CASH gel-water interfacial tension, then with the interfacial tension gradually decreasing as the ratio of aluminum to silicon increases, which implies the existence of optimal Al content. Calculations of lamellar interfacial tension indicate that a higher Al/Si ratio leads to a more homogeneous interfacial structure. Electronic structure analysis reveals that the adsorption of calcium ions at the interface occurs through electrostatic interactions, and the addition of aluminum weakens the localisation of electrons. This study reveals how aluminum incorporation influences the interfacial tension of CASH gel and provides essential guidance for designing concrete with improved resistance to ion transportation.

2. Methodologies

2.1. C-S-H and C-A-S-H modelling

Structure of tobermorite 11 Å model serves as a crystalline template for constructing the molecular structure of CSH and CASH [34]. CSH gels are x-ray amorphous materials that do not have crystal-like long-range ordering, but short-range ordering can be found on the atomic scale [35]. Previous experiments by NMR, synchrotron X-ray diffraction, and others have identified tobermorite is quite similar to CSH gel [36–38]. Moreover, recent research have indicated that among various tobermorite phases, the 11 Å variant most closely resembles the atomic configuration of CSH gel [39,40]. Thus, the selection of 11 Å tobermorite as the basis of the model is generally accepted.

2.2. Force field of simulation

In this study, we used the reactive force field (ReaxFF) to perform molecular dynamics simulations. ReaxFF is capable of modeling and describing chemical reaction processes, including bond formation and breaking between atoms and electron transfer [41,42]. Meanwhile, it realizes the accurate description of chemical reactions by combining empirical parameters and quantum chemical data and is widely used in fields such as gelling materials [43-46]. Taken together the use of Reaxff provides a better description of the

change in CASH gel-water interfacial tension.

2.3. Modelling construction

To explore the effects of the Al phase on the interfacial tension, we first constructed a reasonable CSH/CASH model. The realistic molecular model of CSH/CASH is according to the research of Pellenq et al. [47], in which the calcium to silicon ratio of 1.7 is established through previous measurements [36]. The 11 Å anhydrous tobermorite cell was first supercellularized and expanded to dimensions of 22.32 Å × 22.17 Å × 22.77 Å. Subsequently, the bridging SiO_2 groups in the silica-oxygen tetrahedra were randomly removed based on NMR results [48,49]. This modification resulted in a defective CSH model with ratio of calcium to silicon is 1.65, exhibiting a distribution of $Q^0 = 10.3$ %, $Q^1 = 69$ %, and $Q^2 = 20.7$ %, as shown in Fig. 1a. To construct a saturated CSH model, the defective structure was subjected to Grand Canonical Monte Carlo (GCMC) simulation. The simulation employed the NVT ensemble and achieved equilibrium after 26 ps with a timestep of 1 fs. The CSH's interlayer area was visibly adsorbed with water molecules after equilibration, as illustrated in Fig. 1b. This saturated CSH model provides a basic platform for more detailed investigations into CASH gel's molecular structure.

The CASH model incorporating different aluminum to silicon ratios was established using the previously proposed defective CSH model. Prior to this, it's necessary to identify the preferred binding site for aluminum incorporation within the CSH structure. Previous Si-NMR and Al-NMR studies have demonstrated that tetra-coordinated aluminum, Al (IV), preferentially occupies the bridging sites in the silicate chains of CSH gel [50–53]. Upon aluminum incorporation, the original silicate dimer structure merged into a pentamer, with the resulting charge imbalance compensated by the oxygen atoms' protonation at aluminum-oxygen tetrahedra's bridging sites. As illustrated in Fig. 2a, CASH models were constructed with ratio of aluminum to silicon is 0.1, 0.2, 0.3, and 0.4. The choice of an aluminum-silicon ratio with a wide range of variation enables a better study of whether there is an optimal aluminum content to modulate interfacial tension. This is critical for minimizing solution transport. Then the resulting CASH model was further supercellularized, and 2000 water molecules were added to its surface. Besides, in order to exclude the influence of different surface molecular structures on the interfacial properties, we carried out a unified design of the surface molecular structure at the CASH interface under each system. The final model dimensions were 44.64 Å × 44.34 Å × 105 Å, as shown in Fig. 2b.

2.4. Simulation details

This study utilized the LAMMPS software to perform MD simulations [54]. The NVE ensemble was used to simulate systems with varying Al/Si ratios, enabling full interactions at the CASH gel-water interface. In the NVE ensemble, the number of particles (N), volume (V) and total energy (E) are kept constant. This method is widely used in MD simulations. Simulations employed a Berendsen thermostat set at 298 K, with a timestep of 0.25 fs. Each simulation was run for a total duration of 1 ns to achieve equilibrium. The simulation utilized a reactive force field during the entire process and the three stress components — Pxx, Pyy, and Pzz — were recorded along the Z direction to facilitate subsequent calculations of interfacial tension. As illustrated in Fig. 2b, the equilibrium state reveals the position of the interface after the CASH gel-water react.

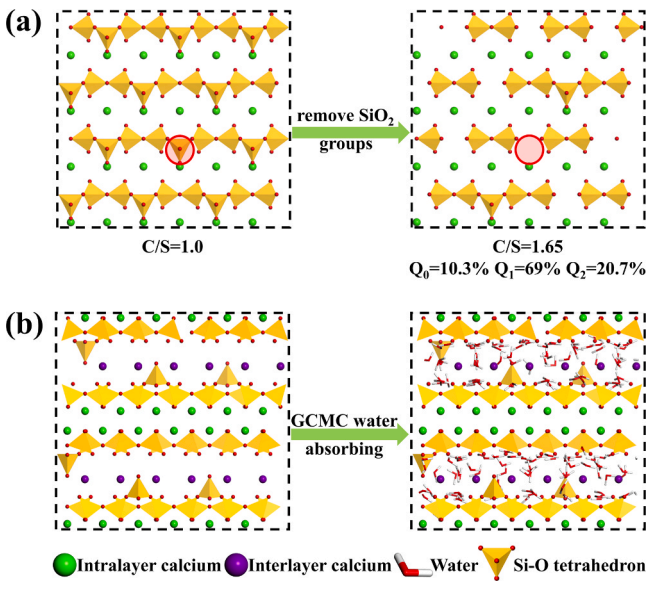

Fig. 1. The schematic diagram of (a) defective CSH modelling. (b) GCMC water-absorbing with Ca/Si= 1.65.

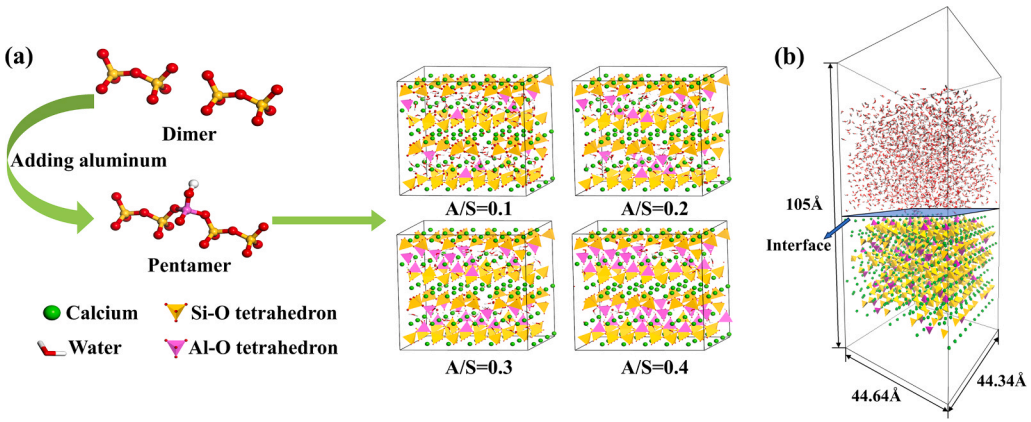

Fig. 2. The schematic diagram of (a) CASH modelling with different Al/Si ratios. (b) modelling was conducted to simulate the interfacial tension and the location of the interface between CASH and water.

2.5. Calculation of interfacial tension

The interfacial tension σ can be determined using the subsequent equation:

$$\sigma = \int \left[P_\gamma - \frac{1}{2}\left(P_\alpha + P_\beta\right) \right] dz \tag{1}$$

Here, σ denotes the interfacial tension, typically expressed in mN/m. P_α, P_β, and P_γ denote the sum of the stresses in the X, Y, and Z axes, correspondingly, for all atoms within the calculated interfacial layer. Based on this equation, the model was laminated into thin layers along the Z direction from bottom to top. The interfacial tension for each layer in the simulated system was determined by calculating the sum of the stresses exerted by all atoms in the X, Y, and Z directions. Using this approach, it enables further investigation of the interfacial tension variations across layers in systems with different Al/Si ratios.

2.6. Quantum chemical calculation

In this study, a quantum chemical computational approach was employed to further analyze the MD simulation results. Upon completion of the MD simulation, the system's equilibrium configuration was obtained, and the corresponding atomic trajectories were extracted. To further analyzed the type of the interfacial interactions and the change in the strength after addition of the aluminum phase, we choose representative surface molecular structures: silicon-oxygen and aluminum-oxygen tetrahedral monomers. The key molecular structures were subjected to single-point (SP) calculations using the CP2K software package [55] to determine the modeled electronic structure.

The SP calculations utilized the PBE functional [56] with the TZVP-MOLOPT-GTH all-electron basis set [57], while Grimme's DFT-D3 (BJ) method [58] was applied to account for dispersion interactions. To enhance the accuracy in describing interfacial interactions, wave function files generated from the SP calculations were analyzed using the Multiwfn software [59]. The reduced

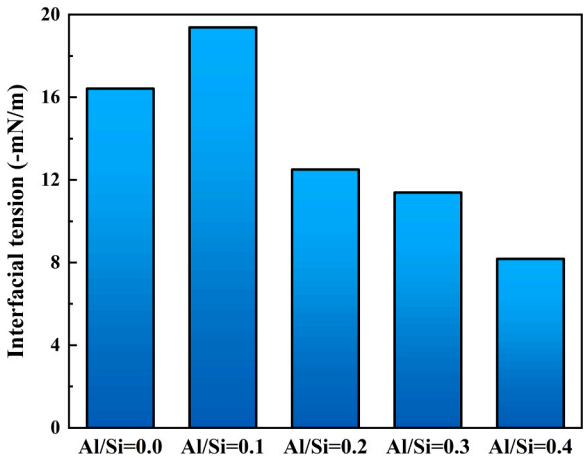

Fig. 3. Histogram of CSH/CASH-water interfacial tension in five types of systems.

density gradient (RDG) and electron localization function (ELF) were calculated to characterize the electronic structure. Additionally, the adsorption energy [60] for different electronic structure systems was calculated using the following equation:

$$E = E_{(ion+sub)} - E_{ion} - E_{sub} \tag{2}$$

Where E_{ion} represents the energy of the adsorbed ion and E_{sub} represents the energy of the substrate, usually expressed in units of eV. Energy calculations were performed on the basis of the optimized molecular structure to avoid errors caused by structural changes during the calculation of adsorption energy.

3. Results and discussion

3.1. Variation of interfacial tension

Fig. 3 presents the calculated interfacial tension values at CASH gel-water reaction interface for five simulated systems. According to the results in Fig. 4, water molecules can penetrate into the interior of the CASH gel to a depth of about 5 Å and show an increasing trend in density at the interface. Therefore, we choose the range of 3 Å above and below the interface as the interfacial region for calculating the interfacial tension. The data indicate that the interfacial tension peaks at a ratio of aluminum to silicon is 0.1, considerably greater than that observed in the other systems. Notably, the initial introduction of aluminum to the CSH structure leads to an increase in interfacial tension. At a ratio of aluminum to silicon is 0.2, however, the interfacial tension decreases dramatically as the Al content gradually rises. As the Al content increases further, the interfacial tension continues to decline. The underlying mechanisms driving this trend require further investigation. To elucidate the observed variation in interfacial tension, we examined two key aspects: the interfacial microstructure and the interfacial interactions.

3.2. Interface microstructure analysis

To investigate the influence of interfacial structure on interfacial tension, we first examined the distribution of 2000 water molecules at the interface. Fig. 4 presents the density distribution of water molecules along the direction perpendicular to the substrate surface. The zero coordinate on the horizontal axis denotes the position of CASH gel–water interaction interface. The findings indicate that water penetrate approximately 5 Å within the CASH gel. There is a rising tendency in the density of water molecules at interface. However, the differences in water distribution across the various systems are not distinctly evident. Consequently, further investigation of the two-dimensional (2D) density distribution of water molecules is required to gain deeper insights.

Fig. 5 presents the 2D density distribution of 2000 water molecules in the XOZ plane. In these visualizations, darker regions indicate higher density and a greater concentration of water molecules. Fig. 5b shows that after aluminum is added to the CSH structure, the quantity of interfacial water molecules is decreasing when compared to Fig. 5a. However, with increasing aluminum content, Fig. 5c–e clearly shows a more concentrated distribution and a progressive rise in the quantity of interfacial water molecules. This trend demonstrates that interfacial tension is related to the distribution of water molecule density. The original CSH gel has more water molecules at interface, but after adding aluminum, the interfacial tension increases, making the interface more hydrophobic and reducing the amount of water molecules. As the aluminum content continues to increase, the interfacial tension decreases, resulting in weaker hydrophobicity and a denser distribution of interfacial water molecules.

To further investigate the role of water in interfacial chemical reactions, we analyzed the water molecules' dipole orientations, as illustrated in Fig. 6. Longer line segments in the figure represent a more concentrated dipole distribution in that direction, indicating a

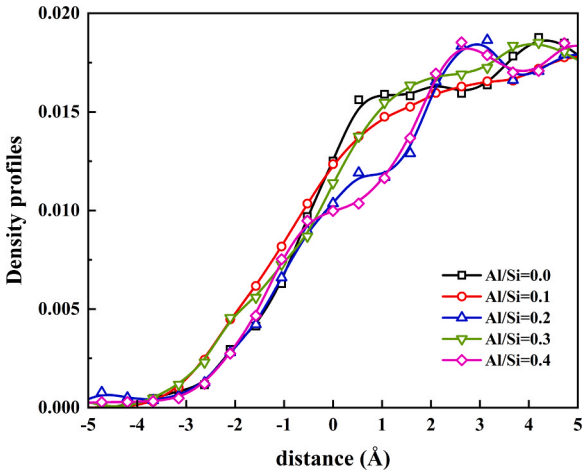

Fig. 4. Density profiles of water molecules in Z direction near the interface.

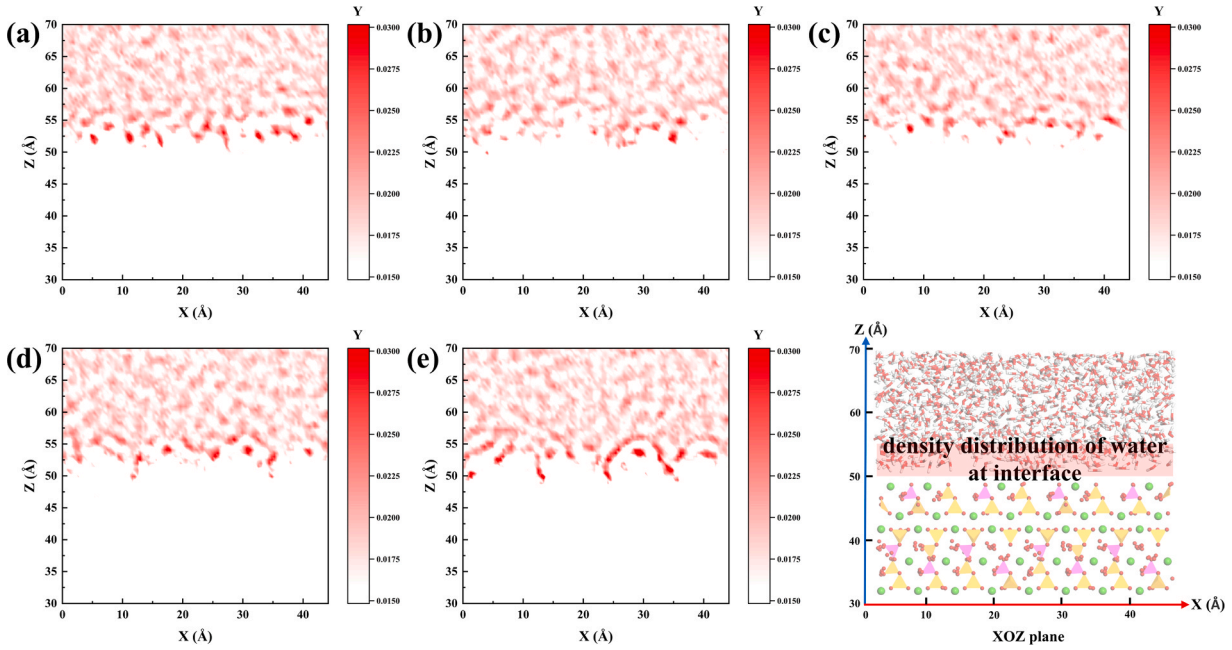

Fig. 5. 2D density profiles of 2000 water molecules of (a) Al/Si= 0, (b) Al/Si= 0.1, (c) Al/Si= 0.2, (d) Al/Si= 0.3, (e) Al/Si= 0.4 systems.

higher degree of water adsorption. Fig. 6a shows that when aluminum is added to CSH, the dipole distribution becomes relatively more uniform, suggesting that most water molecules are in a free state and that aluminum incorporation restricts water molecule adsorption at the interface. The quantity of water adsorbed in the 270° direction grows steadily from a ratio of aluminum to silicon is 0.2 onwards, as seen in Fig. 6b–d. This observation indicates that more water molecules are actively involved in the reaction at the interface when aluminum to silicon ratio is higher.

To investigate changes in the interfacial structure, the systems with different Al/Si ratios were laminated into several thin layers in a direction perpendicular to the substrate. We obtained a graphic illustrating the variation of interfacial tension for lamellar systems with different Al/Si ratios by calculating it for each thin layer. The spatial fluctuations of the lamellar interfacial tension curves are directly related to local density inhomogeneities. Moreover, the changes in the interfacial properties induced by different amounts of aluminum doping can also be captured by the lamellar interfacial tension curves. This method has been widely validated for characterizing the structural properties of interfaces [61-63]. Fig. 7b shows that the interfacial tension curves for the lamellar systems exhibit minimal change compared to those in Fig. 7a. This indicates that the interfacial structure remains relatively unchanged at a ratio of aluminum to silicon is 0.1, which is consistent with the small increase in interfacial tension observed upon the initial addition of aluminum to the CSH structure. However, when the aluminum to silicon ratio reaches 0.2, as shown in Fig. 7c, the curve shows distinct fluctuations, indicating a significant change in the interfacial structure. This, in turn, results in a marked change in interfacial tension. An intriguing observation is that as aluminum content continues to increase, the curve becomes more distinct, as seen in Fig. 7d–e. This suggests that a higher aluminum to silicon ratio result in a more homogeneous interfacial structure and a corresponding decrease in interfacial tension.

3.3. Molecular interaction analysis

Interactions between atoms and molecules at the interface also influence the interfacial tension. Particles' probability distributions at different distances from a reference particle can be measured using the Radial Distribution Function (RDF), thereby indicating the strength of bonds between specific atoms. As depicted in Fig. 8a, the RDF between Ca and aluminum-oxygen tetrahedra in systems with varying Al/Si ratios exhibits peaks at 3.1 Å. The RDF peak is significantly higher in systems with aluminum to silicon ratio is 0.1 compared to the others, suggesting stronger interactions between Ca and aluminum-oxygen tetrahedra. In contrast, as the aluminum content increases, the RDF peak decreases, indicating weaker interactions. Based on these results, it suggests that the interfacial interaction is enhanced when aluminum is initially added to CSH, preventing calcium from detaching easily from the CASH surface. However, as the aluminum content increases, the interaction between Ca and aluminum-oxygen tetrahedra weakens, making it more likely for calcium to detach from the surface. Similar trends are observed in Fig. 8b, where the peak for the Ca-$O_{(water)}$ bond increases with higher aluminum content, indicating stronger bonding. This suggests that as aluminum content increases, calcium is more likely to enter the water and participate in reactions. In Fig. 9a and Fig. 9b, the peaks for Si-$O_{(water)}$ and Al-$O_{(water)}$ are largest when the Al/Si ratio is 0.1. The peaks decrease significantly at an Al/Si ratio of 0.2 but gradually rise thereafter. This indicates a weakening of the interfacial interactions at a ratio of aluminum to silicon is 0.2, accompanied by a decrease in the strength of Si-$O_{(water)}$ and Al-$O_{(water)}$ bonds. As the aluminum content increases, the bond strength gradually improves. Overall, calcium is the main determinant of the

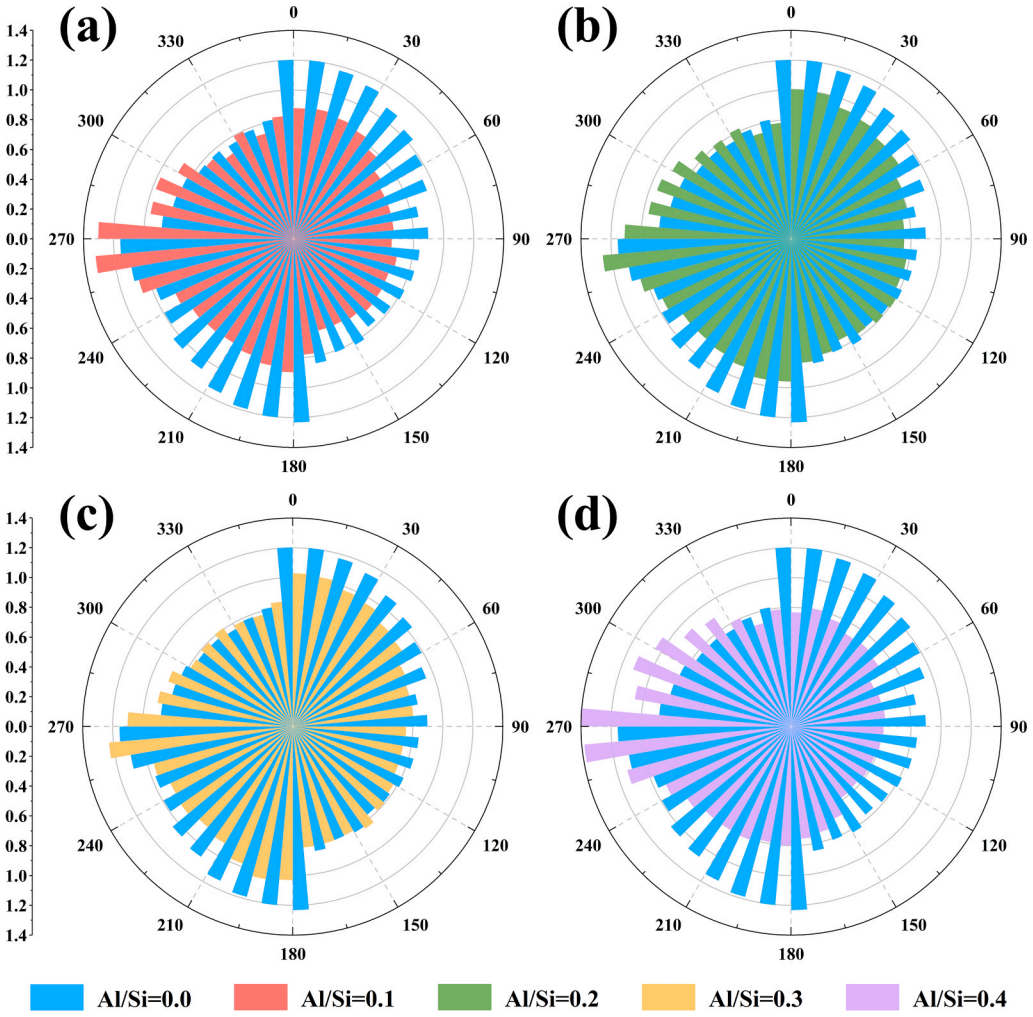

Fig. 6. The dipole direction distribution of H_2O with (a) Al/Si= 0.1, (b) Al/Si= 0.2, (c) Al/Si= 0.3, (d) Al/Si= 0.4 systems.

CASH-water interface interaction.

The time correlation function (TCF) is used to characterize the stability of chemical bonds. As shown in Fig. 10a, the stability of the Ca-$O_{(water)}$ bond gradually decreases with increasing aluminum content. This suggests that as more calcium enters the water and participates in reactions, the Ca-$O_{(water)}$ bond becomes less stable and more prone to breaking. For the Si-$O_{(water)}$ bond, the trend in stability mirrors that observed in the RDF, as depicted in Fig. 10b. When aluminum to silicon ratio is 0.2, the bond's stability decreases significantly, resulting in the breaking of more bonds. However, as the aluminum content continues to increase, the stability of the Si-$O_{(water)}$ bond gradually improves. Fig. 10c illustrates that the Al-$O_{(water)}$ bond remains poorly stabilized across all Al/Si ratio systems. This indicates that aluminum promotes active participation in the interfacial reaction, leading to more frequent breaking of the Al-$O_{(water)}$ bond.

In addition to studying chemical bonds' breakage using the TCF, the bonding time evolution (BTE) was employed to assess the number of bonds broken and regenerated. The magnitude of the vertical coordinate, P(t), indicates the ratio of the number of a specific chemical bond at time t to the initial number of bonds, allowing for the evaluation of the bond's state at time t. If $P(t) > 1$, it indicates that the number of new bond formations exceeds the number of bond breaks. Conversely, if $P(t) < 1$, it suggests that the number of newly formed bonds is fewer than the number of broken bonds. Fig. 11a shows that for an aluminum to silicon ratio of 0.1, P(t) is consistently greater than 1, which means that new bonds are being formed for the Ca-$O_{(water)}$ bond at a faster rate than old ones are being broken. For the systems with other Al/Si ratios, the P(t) values fluctuate slightly around 1, suggesting that the Ca-$O_{(water)}$ bond is relatively weaker compared to the system with a ratio of aluminum to silicon is 0.1. In Fig. 11b, P(t) is generally less than 1 when the ratio of aluminum to silicon is 0.2, implying that more bonds are broken than are formed between Si and $O_{(water)}$. For the other systems, the P(t) values show minor fluctuations around 1. In Fig. 11c, for the Al-$O_{(water)}$ bond, the P(t) value remains near 1 across all Al/Si ratios, suggesting that the Al-$O_{(water)}$ bond is weaker in comparison.

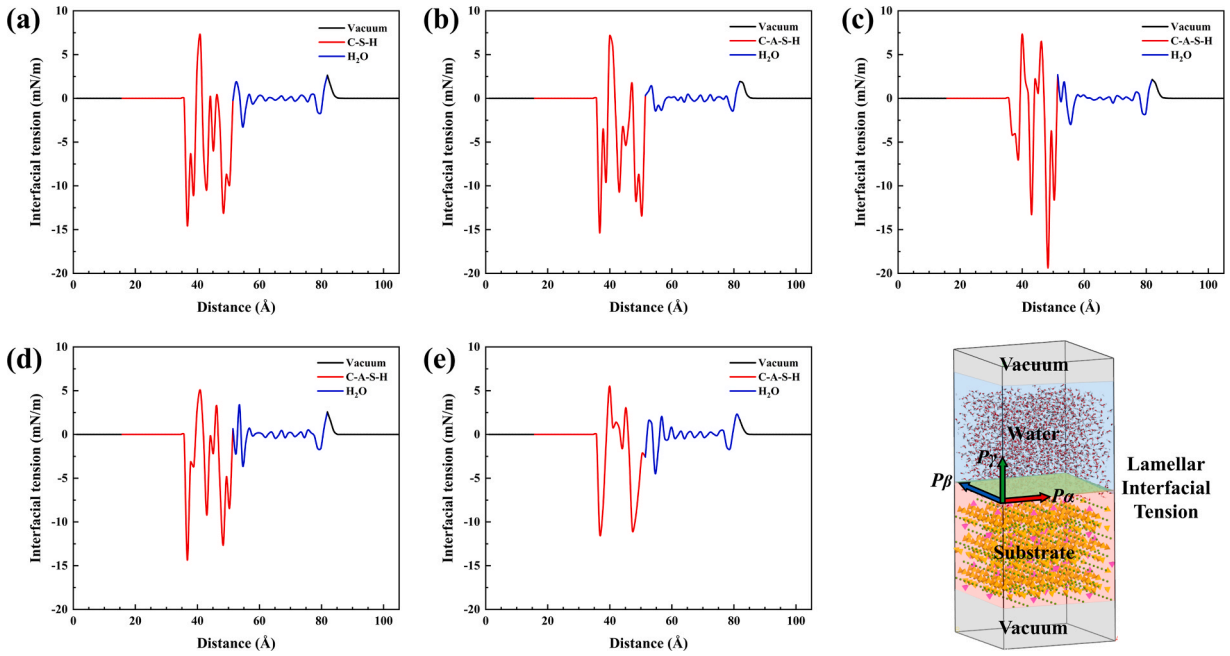

Fig. 7. Lamellar interfacial tension curves of (a) Al/Si= 0, (b) Al/Si= 0.1, (c) Al/Si= 0.2, (d) Al/Si= 0.3, (e) Al/Si= 0.4 systems.

3.4. Adsorption energy analysis

To further investigate the changes in the interface's adsorption strength of calcium ions, we constructed and optimized the key molecular structures of silicon and aluminum, as depicted in Fig. 12a-b. Subsequently, we calculated the adsorption energy of calcium ions for the two different molecular structures using Eq. (2), with the results presented in Fig. 12c. The findings demonstrate that the molecular structure containing the aluminum phase exhibits a higher adsorption energy for calcium ions compared to the silicon system. This is consistent with the molecular interaction analysis from the previous section, where the introduction of the aluminum phase enhances the adsorptive nature of the interface for calcium ions, making it more difficult for the calcium ions to detach from the surface and participate in reactions.

3.5. Electronic structural information

The interactions were identified by the electronic structures. We use Reduced Density Gradient analysis to reveal that non-bonding interactions play a pivotal role in calcium ion adsorption at the interface. Fig. 13 shows the RDG isosurfaces and scatter plots depicting the adsorption of calcium ions onto the silica-oxygen and aluminum-oxygen tetrahedral monomer molecular structures. The red, blue, and green isosurface regions in the figures correspond to steric hindrance effects, hydrogen bonding or electrostatic interactions, and van der Waals interactions, respectively. As shown in Fig. 13c, the silica-oxygen tetrahedral monomer molecular structure adsorbs calcium ions through strong electrostatic interactions of approximately −0.041 and −0.047, which correspond to the two blue isosurface regions in Fig. 13a. Notably, no chemical bonds are formed during this adsorption, indicating that this is a physical adsorption process. A similar conclusion is drawn from the aluminum-oxygen tetrahedral monomer molecular structure. As shown in Fig. 13d, the aluminum-oxygen tetrahedral monomer molecular structure adsorbs calcium ions via strong electrostatic interactions of approximately −0.033 and −0.036, corresponding to the upper two blue isosurface regions in Fig. 13b. Once again, no chemical bonds are generated, confirming that this is also a physical adsorption process. Based on the RDG results, physical adsorption controls the calcium ion adsorption by both the silicon and aluminum molecule structures at the interface, with strong electrostatic interactions but no chemical bond formation. This is different from the interactions involving chemical bonding between calcium ions and water obtained from previous analyses of results such as RDF. Fundamentally, the adsorption of calcium ions on the CASH gel surface and the reaction of calcium ions with water are two different processes, and the two are not related in terms of the type of interaction. However, this further confirms the complexity and diversity of interfacial interactions.

To further investigate the understanding of how the two molecular systems' electronic structures differ when adsorbing calcium ions, we analyzed the Electron Localization Function. The ELF provides insights into the structure of atomic shells and specific chemical bond characteristics. Higher ELF values indicate greater stability in the corresponding isosurface region, with restricted internal electron movement and more localized electrons. Conversely, lower ELF values suggest weaker electron localization and a higher likelihood of electron movement. Fig. 14 displays the local electronic structure that forms when oxygen is adsorbed onto calcium ions at two distinct sites within the molecular structures of silicon and aluminum, respectively. In Fig. 14a2-d2, the four peaks

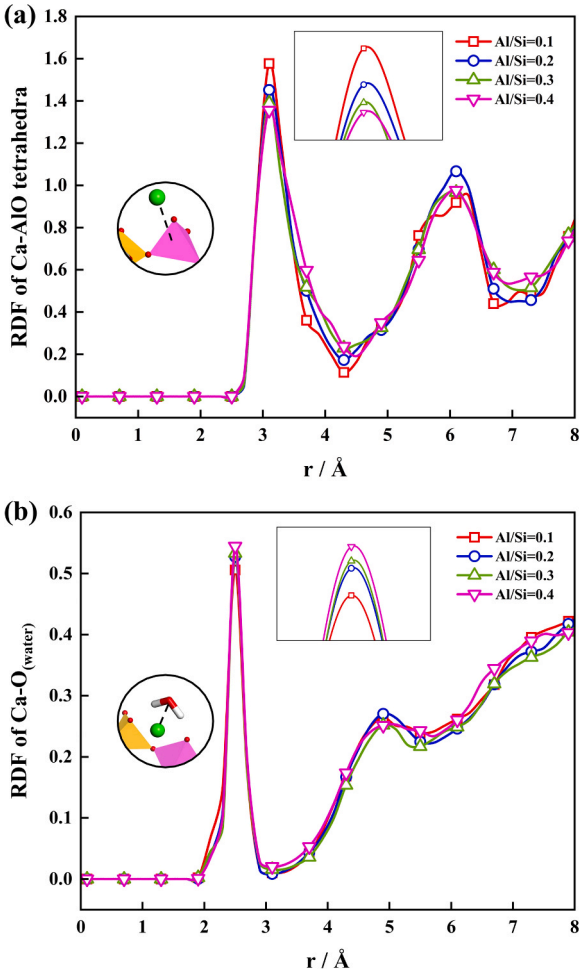

Fig. 8. The RDF of (a) Ca-AlO tetrahedra, (b) Ca-$O_{(water)}$.

from left to right correspond to: (1) electrons from calcium ions, (2) shared electrons provided by calcium ions to the Ca-O pairs, (3) shared electrons provided by oxygen to the Ca-O pairs, and (4) electrons from oxygen. From these figures, it is evident that in the case of electrostatic interactions, the ELF values are close to 0, which demonstrates weak electron localization. This weak localization inhibits the formation of covalent bonds. Notably, in Fig. 14c2 and d2, compared to Fig. 14a2 and b2, the ELF values are lower and the lone-pair domains are larger at the positions indicated by the blue arrows in the isosurface plots. This suggests that in the aluminum-oxygen tetrahedral monomer molecular structure, the lone-pair domains are less localized, allowing for more freedom of electronic motion. These results indicate that the oxygen atom in the aluminum-oxygen tetrahedral monomer molecular structure is more weakly electronically localized to the calcium ion, which is in agreement with the RDG analysis from the previous section that identified an electrostatic interaction for calcium ion adsorption.

4. Conclusion

In this study, the CASH gel-water interfacial tension was systematically investigated through molecular dynamics simulations, focusing on varying Al/Si ratios. The magnitude of interfacial tension is influenced by a combination of interfacial structural changes and molecular interactions at the interface. These changes were observed by analyzing the interfacial tension across layers, while the molecular interactions at the interface were further explored using functional images and quantum chemical calculations. As follows are the main conclusions:

(1) Aluminum incorporation leads to a small increase in interfacial tension between CASH gel and water. However, as the Al/Si ratio increases, the interfacial tension gradually decreases.

(2) The interfacial structure remains largely unchanged when aluminum is first introduced into CSH. A significant structural change occurs when the aluminum to silicon ratio reaches 0.2, with larger Al/Si ratios leading to a more homogeneous interfacial structure.

(3) Interfacial interactions are predominantly influenced by calcium. The incorporation of aluminum impedes the detachment of

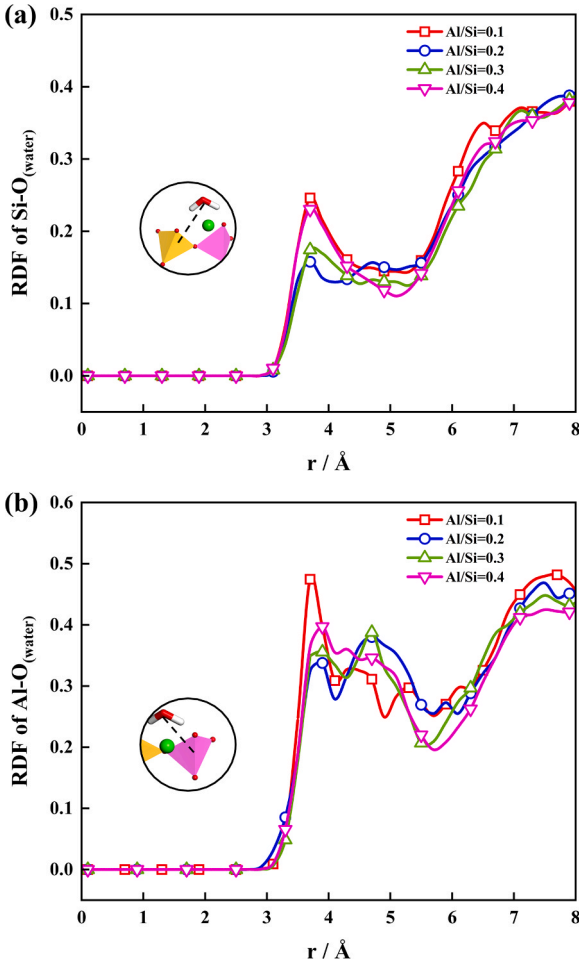

Fig. 9. The RDF of (a) Si-$O_{(water)}$, (b) Al-$O_{(water)}$.

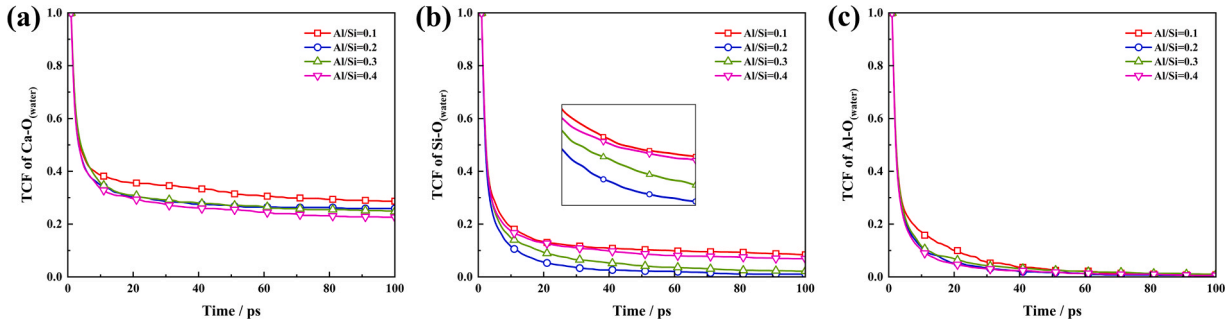

Fig. 10. The TCF of (a) Ca-$O_{(water)}$, (b) Si-$O_{(water)}$, (c) Al-$O_{(water)}$.

calcium from the surface of CASH, while increasing the ratio of aluminum to silicon facilitates calcium entry into the water and strengthens its binding with water molecules.

(4) The addition of aluminum enhances the interfacial adsorption energy of calcium ions, while simultaneously weakening the localization of electrons in the lone-pair domains. The interfacial adsorption of calcium ions is a physical process driven primarily by electrostatic interactions.

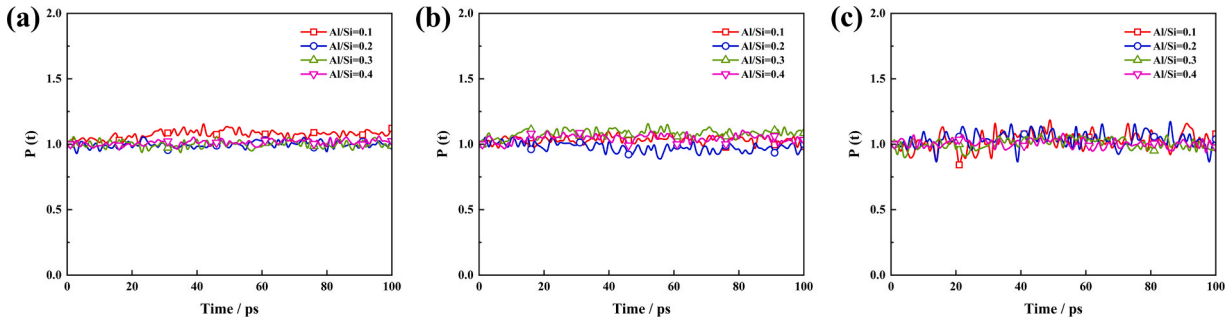

Fig. 11. The BTE of (a) Ca-$O_{(water)}$, (b) Si-$O_{(water)}$, (c) Al-$O_{(water)}$.

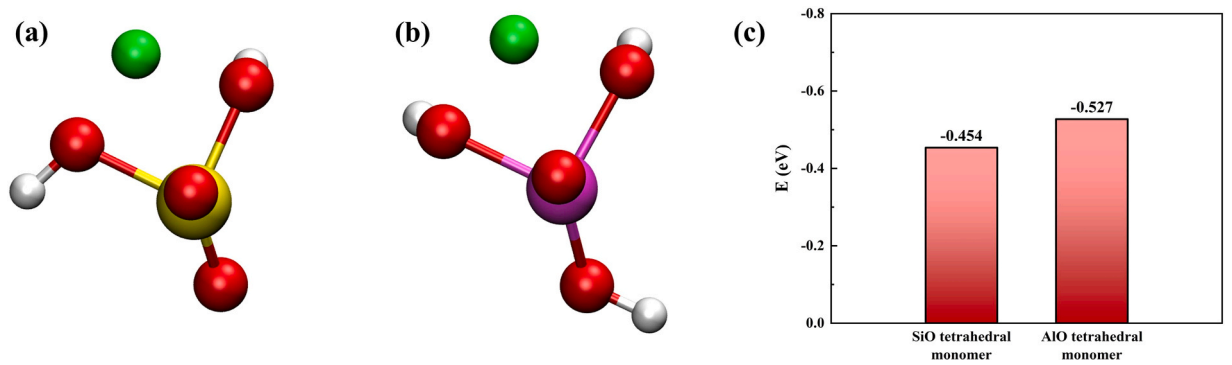

Fig. 12. The schematic of key optimized molecular structure at the interface of (a) silica-oxygen tetrahedral monomer, (b) aluminum-oxygen tetrahedral monomer. The histogram of (c) adsorption energy of calcium ions by two key interfacial molecular structures.

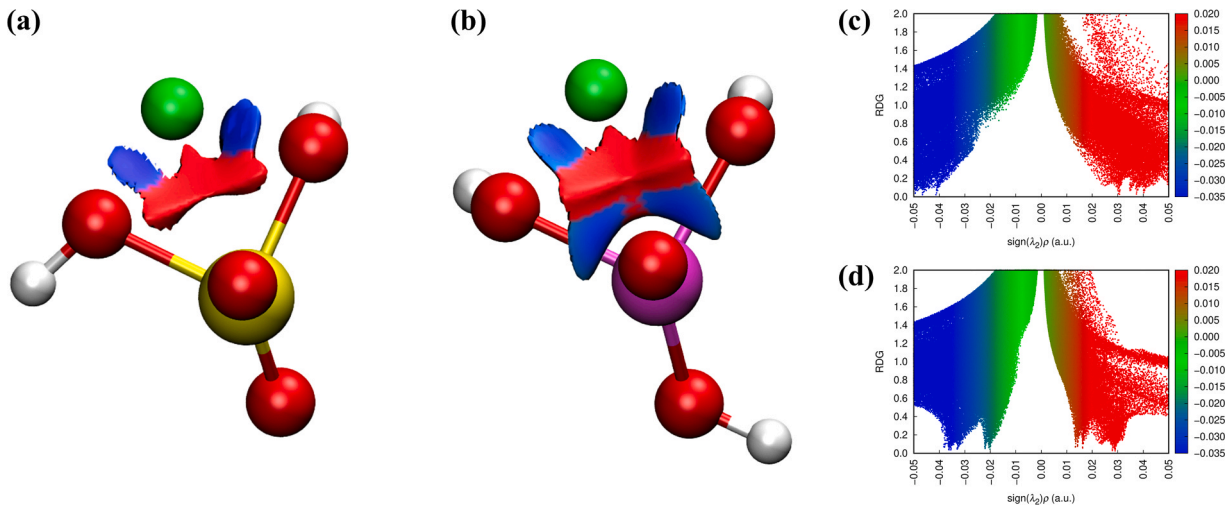

Fig. 13. The schematic of RDG isosurfaces with (a) silica-oxygen tetrahedral monomer molecular structure and (b) aluminum-oxygen tetrahedral monomer molecular structure at the interface. The scatter plots of RDG with (c) silica-oxygen tetrahedral monomer molecular structure and (d) aluminum-oxygen tetrahedral monomer molecular structure at the interface.

CRediT authorship contribution statement

Xiangming Zhou: Writing – review & editing, Supervision, Methodology, Conceptualization. **Dongshuai Hou:** Writing – review & editing, Data curation. **Muhan Wang:** Writing – review & editing, Supervision, Methodology, Conceptualization. **Pan Wang:** Writing – review & editing, Data curation. **Yue Zhang:** Writing – review & editing, Data curation, Conceptualization. **Wenhao Xia:** Writing – original draft, Data curation. **Yihan Wang:** Data curation.

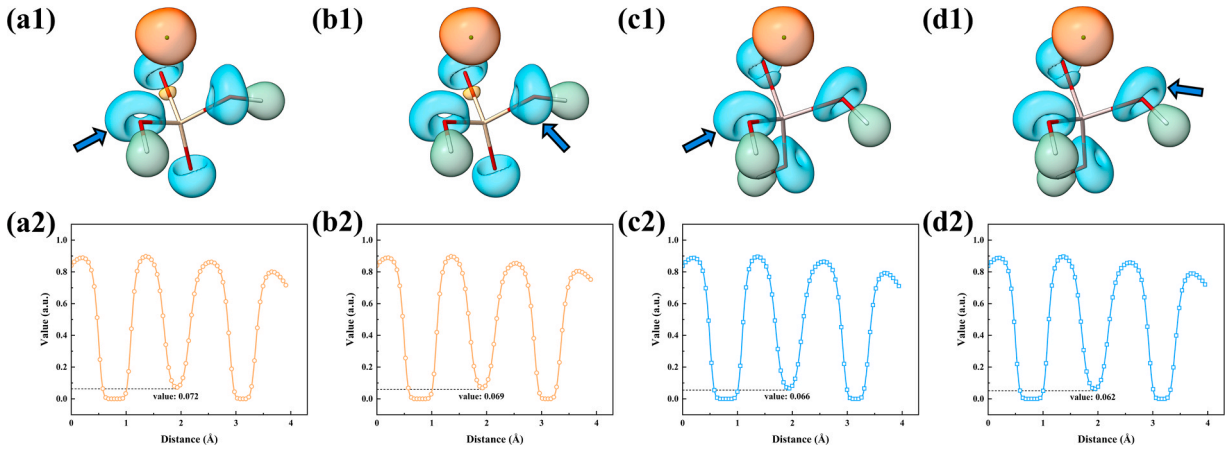

Fig. 14. The schematic of ELF isosurfaces with calcium ion on (a1) oxygen I and (b1) oxygen II in silica-oxygen tetrahedral monomer molecular structure, (c1) oxygen I and (d1) oxygen II in aluminum-oxygen tetrahedral monomer molecular structure. The curves of ELF with calcium ion on (a2) oxygen I and (b2) oxygen II in silica-oxygen tetrahedral monomer molecular structure, (c2) oxygen I and (d2) oxygen II in aluminum-oxygen tetrahedral monomer molecular structure. The oxygen lone pair domain is represented by cyan, the hydrogen lone pair domain by green, and the calcium ion lone pair domain by orange.

Declaration of Competing Interest

No conflict of interest is declared.

Acknowledgment

M. W. and D. H. financial support from the National key research and development project 2022YFE0133800, the National Natural science foundation of China under Grant U2006224, 52308263, Shandong Province Natural Science Foundation under Grant ZR2022YQ55, Shandong Provincial Education Department under Grant 2023KJ320, Qingdao Research Program 16–5–1–96-jch, 111 Project TMduracon20220022. Newton International Fellowship NIF\R1\242498.

Data availability

The data that has been used is confidential.

References

[1] Z. Li, X. Zhou, H. Ma, D. Hou, Advanced Concrete Technology, John Wiley & Sons, 2022.
[2] S.W. Tang, Y. Yao, C. Andrade, Z.J. Li, Recent durability studies on concrete structure, Cem. Concr. Res. 78 (2015) 143–154.
[3] X. Shi, N. Xie, K. Fortune, J. Gong, Durability of steel reinforced concrete in chloride environments: an overview, Constr. Build. Mater. 30 (2012) 125–138.
[4] Q.F. Liu, G.L. Feng, J. Xia, J. Yang, L.Y. Li, Ionic transport features in concrete composites containing various shaped aggregates: a numerical study, Compos. Struct. 183 (2018) 371–380.
[5] P.K. Mehta, P. Monteiro, Concr. Microstruct. Prop. Mater. (2006).
[6] L. Hanžič, L. Kosec, I. Anžel, Capillary absorption in concrete and the Lucas–Washburn equation, Cem. Concr. Compos. 32 (1) (2010) 84–91.
[7] D. Hou, H. Ma, Y. Zhu, Z. Li, Calcium silicate hydrate from dry to saturated state: structure, dynamics and mechanical properties, Acta Mater. 67 (2014) 81–94.
[8] R. Di Mundo, C. Labianca, G. Carbone, M. Notarnicola, Recent advances in hydrophobic and icephobic surface treatments of concrete, Coatings 10 (5) (2020) 449.
[9] X. Pan, Z. Shi, C. Shi, T.C. Ling, N. Li, A review on concrete surface treatment part I: types and mechanisms, Constr. Build. Mater. 132 (2017) 578–590.
[10] M. Wang, S. Yu, C. Liu, P. Wang, Y. Zhang, X. Wang, D. Hou, Design of high chloride-resistant passivation films: From synthesis to the mechanisms of nano-generation, Corrosion Science 244 (2025) 112656.
[11] A. Arabzadeh, H. Ceylan, S. Kim, K. Gopalakrishnan, A. Sassani, S. Sundararajan, P.C. Taylor, Superhydrophobic coatings on portland cement concrete surfaces, Constr. Build. Mater. 141 (2017) 393–401.
[12] W. Zheng, W.G. Chen, T. Feng, W.Q. Li, X.T. Liu, L.L. Dong, Y.Q. Fu, Enhancing chloride ion penetration resistance into concrete by using graphene oxide reinforced waterborne epoxy coating, Prog. Org. Coat. 138 (2020) 105389.
[13] X.D. Zhu, A. Zaoui, W. Sekkal, Molecular-scale insight into improved waterproofing of cement paste by protective epoxy resins nano-coating, Powder Technol. 426 (2023) 118679.
[14] S. Mindess, Ed. Developments in the Formulation and Reinforcement of Concrete, Woodhead Publishing, 2019.
[15] H.S. Wong, R. Barakat, A. Alhilali, M. Saleh, C.R. Cheeseman, Hydrophobic concrete using waste paper sludge ash, Cem. Concr. Res. 70 (2015) 9–20.
[16] Z.Y. Qu, Q.L. Yu, Synthesizing super-hydrophobic ground granulated blast furnace slag to enhance the transport property of lightweight aggregate concrete, Constr. Build. Mater. 191 (2018) 176–186.
[17] F. Wang, S. Lei, J. Ou, W. Li, Effect of PDMS on the waterproofing performance and corrosion resistance of cement mortar, Appl. Surf. Sci. 507 (2020) 145016.
[18] M.J. Abdolhosseini Qomi, F.J. Ulm, R.J.M. Pellenq, Evidence on the dual nature of aluminum in the calcium-silicate-hydrates based on atomistic simulations, J. Am. Ceram. Soc. 95 (3) (2012) 1128–1137.
[19] D. Hou, T. Li, P. Wang, Molecular dynamics study on the structure and dynamics of NaCl solution transport in the nanometer channel of C-A-S-H gel, ACS Sustain. Chem. Eng. 6 (7) (2018) 9498–9509.

[20] D. Hou, T. Li, Influence of aluminates on the structure and dynamics of water and ions in the nanometer channel of calcium silicate hydrate (C–S–H) gel, Phys. Chem. Chem. Phys. 20 (4) (2018) 2373–2387.
[21] B. Lothenbach, K. Scrivener, R.D. Hooton, Supplementary cementitious materials, Cem. Concr. Res. 41 (12) (2011) 1244–1256.
[22] F. Puertas, M. Palacios, H. Manzano, J.S. Dolado, A. Rico, J. Rodríguez, A model for the C-A-S-H gel formed in alkali-activated slag cements, J. Eur. Ceram. Soc. 31 (12) (2011) 2043–2056.
[23] E. Gartner, H. Hirao, A review of alternative approaches to the reduction of CO2 emissions associated with the manufacture of the binder phase in concrete, Cem. Concr. Res. 78 (2015) 126–142.
[24] C. Gunasekara, Z. Zhou, D.W. Law, M. Sofi, S. Setunge, P. Mendis, Microstructure and strength development of quaternary blend high-volume Fly ash concrete, J. Mater. Sci. 55 (2020) 6441–6456.
[25] K.P. Sethy, D. Pasla, U.C. Sahoo, Utilization of high volume of industrial slag in self compacting concrete, J. Clean. Prod. 112 (2016) 581–587.
[26] P. Rucker-Gramm, R.E. Beddoe, Effect of moisture content of concrete on water uptake, Cem. Concr. Res. 40 (1) (2010) 102–108.
[27] J.D. Berry, M.J. Neeson, R.R. Dagastine, D.Y. Chan, R.F. Tabor, Measurement of surface and interfacial tension using pendant drop tensiometry, J. Colloid Interface Sci. 454 (2015) 226–237.
[28] Q. Luo, J. Huang, Mechanisms and critical technologies of transport inhibitor agent (TIA) throughout C-S-H Nano-Channels, Materials 15 (2) (2022) 515.
[29] D. Hou, Q. Yang, P. Wang, M. Wang, Y. Zhang, X. Wang, J. Zhang, Concentration-induced wettability alteration of nanoscale NaCl solution droplets on the C-S-H surface, Phys. Chem. Chem. Phys. 23 (12) (2021) 7449–7461.
[30] G. Yang, X. Chen, J. Xu, Molecular dynamics simulation of interfacial mechanical properties of crumb rubber concrete, Constr. Build. Mater. 438 (2024) 137336.
[31] Q. Han, Y. Yang, J. Zhang, J. Yu, D. Hou, B. Dong, H. Ma, Insights into the interfacial strengthening mechanism of waste rubber/cement paste using polyvinyl alcohol: experimental and molecular dynamics study, Cem. Concr. Compos. 114 (2020) 103791.
[32] J. Du, Y. Bu, Z. Shen, Interfacial properties and nanostructural characteristics of epoxy resin in cement matrix, Constr. Build. Mater. 164 (2018) 103–112.
[33] F. Sanchez, L. Zhang, Interaction energies, structure, and dynamics at functionalized graphitic structure–liquid phase interfaces in an aqueous calcium sulfate solution by molecular dynamics simulation, Carbon 48 (4) (2010) 1210–1223.
[34] S.A. Hamid, The crystal structure of the 11Å natural tobermorite Ca2. 25 [Si3O7. 5 (OH) 1.5]· 1H2O, Z. F. üR. Krist. Cryst. Mater. 154 (3-4) (1981) 189–198.
[35] E. Duque-Redondo, P.A. Bonnaud, H. Manzano, A comprehensive review of C-S-H empirical and computational models, their applications, and practical aspects, Cem. Concr. Res. 156 (2022) 106784.
[36] A.J. Allen, J.J. Thomas, H.M. Jennings, Composition and density of nanoscale calcium–silicate–hydrate in cement, Nat. Mater. 6 (4) (2007) 311–316.
[37] E. Fratini, F. Ridi, S.H. Chen, P. Baglioni, Hydration water and microstructure in calcium silicate and aluminate hydrates, J. Phys. Condens. Matter 18 (36) (2006). S2467.
[38] L.B. Skinner, S.R. Chae, C.J. Benmore, H.R. Wenk, P.J.M. Monteiro, Nanostructure of calcium silicate hydrates in cements, Phys. Rev. Lett. 104 (19) (2010) 195502.
[39] C. Biagioni, S. Merlino, E. Bonaccorsi, The tobermorite supergroup: a new nomenclature, Mineral. Mag. 79 (2) (2015) 485–495.
[40] A. Cuesta, J.D. Zea-Garcia, D. Londono-Zuluaga, A.G. De la Torre, I. Santacruz, O. Vallcorba, M.A. Aranda, Multiscale understanding of tricalcium silicate hydration reactions, Sci. Rep. 8 (1) (2018) 8544.
[41] A.C. Van Duin, S. Dasgupta, F. Lorant, W.A. Goddard, ReaxFF: a reactive force field for hydrocarbons, J. Phys. Chem. A 105 (41) (2001) 9396–9409.
[42] T.P. Senftle, S. Hong, M.M. Islam, S.B. Kylasa, Y. Zheng, Y.K. Shin, A.C. Van Duin, The ReaxFF reactive force-field: development, applications and future directions, npj Comput. Mater. 2 (1) (2016) 1–14.
[43] D. Hou, Z. Lu, T. Zhao, Q. Ding, Reactive molecular simulation on the ordered crystal and disordered glass of the calcium silicate hydrate gel, Ceram. Int. 42 (3) (2016) 4333–4346.
[44] D. Hou, T. Yang, J. Tang, S. Li, Reactive force-field molecular dynamics study on graphene oxide reinforced cement composite: functional group de-protonation, interfacial bonding and strengthening mechanism, Phys. Chem. Chem. Phys. 20 (13) (2018) 8773–8789.
[45] W. Sun, C. Liu, F. Hong, P. Wang, Y. Zhang, X. Wang, M. Wang, Deterioration of passivation film caused by carbonation in reinforced concrete: An electrochemical and nanoscale perspectives, Journal of Building Engineering 106 (2025) 112524.
[46] S. Yu, Q. Liu, F. Hong, P. Wang, D. Hou, M. Wang, Crystal structure-dependent evaluation of chloride ions resistance of iron passivation film in reinforced concrete at the nanoscale, Journal of Building Engineering 95 (2024) 110179.
[47] R.J.M. Pellenq, A. Kushima, R. Shahsavari, K.J. Van Vliet, M.J. Buehler, S. Yip, F.J. Ulm, A realistic molecular model of cement hydrates, Proc. Natl. Acad. Sci. 106 (38) (2009) 16102–16107.
[48] J.J. Chen, J.J. Thomas, H.F. Taylor, H.M. Jennings, Solubility and structure of calcium silicate hydrate, Cem. Concr. Res. 34 (9) (2004) 1499–1519.
[49] X. Cong, R.J. Kirkpatrick, 29Si MAS NMR study of the structure of calcium silicate hydrate, Adv. Cem. Based Mater. 3 (3-4) (1996) 144–156.
[50] M.D. Andersen, H.J. Jakobsen, J. Skibsted, Incorporation of aluminum in the calcium silicate hydrate (C− S− H) of hydrated portland cements: a high-field 27Al and 29Si MAS NMR investigation, Inorg. Chem. 42 (7) (2003) 2280–2287.
[51] M.D. Andersen, H.J. Jakobsen, J. Skibsted, A new aluminium-hydrate species in hydrated portland cements characterized by 27Al and 29Si MAS NMR spectroscopy, Cem. Concr. Res. 36 (1) (2006) 3–17.
[52] I.G. Richardson, A.R. Brough, R. Brydson, G.W. Groves, C.M. Dobson, Location of aluminum in substituted calcium silicate hydrate (C-S-H) gels as determined by 29Si and 27Al NMR and EELS, J. Am. Ceram. Soc. 76 (9) (1993) 2285–2288.
[53] X. Pardal, F. Brunet, T. Charpentier, I. Pochard, A. Nonat, 27Al and 29Si solid-state NMR characterization of calcium-aluminosilicate-hydrate, Inorg. Chem. 51 (3) (2012) 1827–1836.
[54] S. Plimpton, P. Crozier, A. Thompson, LAMMPS-large-scale atomic/molecular massively parallel simulator, sandia national laboratories, 2007, Uncertain. Quantif. Mater. Model. 37 (2007).
[55] T.D. Kühne, M. Iannuzzi, M. Del Ben, V.V. Rybkin, P. Seewald, F. Stein, J. Hutter, CP2K: an electronic structure and molecular dynamics software package-quickstep: efficient and accurate electronic structure calculations, J. Chem. Phys. 152 (19) (2020).
[56] B.H.L.B. Hammer, L.B. Hansen, J.K. Nørskov, Improved adsorption energetics within density-functional theory using revised Perdew-Burke-Ernzerhof functionals, Phys. Rev. B 59 (11) (1999) 7413.
[57] J. Laun, D. Vilela Oliveira, T. Bredow, Consistent Gaussian basis sets of double-and triple-zeta valence with polarization quality of the fifth period for solid-state calculations, J. Comput. Chem. 39 (19) (2018) 1285–1290.
[58] J. Moellmann, S. Grimme, DFT-D3 study of some molecular crystals, J. Phys. Chem. C 118 (14) (2014) 7615–7621.
[59] T. Lu, F. Chen, Multiwfn: a multifunctional wavefunction analyzer, J. Comput. Chem. 33 (5) (2012) 580–592.
[60] C. Xie, D. Yan, W. Chen, Y. Zou, R. Chen, S. Zang, S. Wang, Insight into the design of defect electrocatalysts: from electronic structure to adsorption energy, Mater. Today 31 (2019) 47–68.
[61] F. Taherian, V. Marcon, N.F. van der Vegt, F. Leroy, What is the contact angle of water on graphene? Langmuir 29 (5) (2013) 1457–1465.
[62] D. Hou, Z. Li, T. Zhao, Reactive force field simulation on polymerization and hydrolytic reactions in calcium aluminate silicate hydrate (C–A–S–H) gel: structure, dynamics and mechanical properties, RSC Adv. 5 (1) (2015) 448–461.
[63] T. Lv, J. Zhang, D. Hou, W.J. Long, B. Dong, Mechanical-thermal activated dredged sludge as a supplementary cementitious material: Microstructure reconstruction and pozzolanic activity enhancement, Construction and Building Materials 476 (2025) 141256.